May 5, 2023

Frozen hydrometeor terminal fall velocity dependence on particle habit and riming as observed by vertically-pointing radars

Sergey Y. Matrosov

Cooperative Institute for Research in Environmental Sciences, University of Colorado, and NOAA Physical Sciences Laboratory, Boulder, Colorado

Corresponding author address: Sergey Y. Matrosov, R/PSDN, 325 Broadway, Boulder, CO 80305.
E-mail: sergey.matrosov@noaa.gov

Early Online Release: This preliminary version has been accepted for publication in *Journal of Applied Meteorology and Climatology*, may be fully cited, and has been assigned DOI 10.1175/JAMC-D-23-0002.1. The final typeset copyedited article will replace the EOR at the above DOI when it is published.

Abstract

Vertically-pointing K_a-band radar measurements are used to derive fall velocity – reflectivity factor ($V_t=aZ_e^b$) relations for frozen hydrometeor populations of different habits during snowfall events observed at Oliktok Point, Alaska, and at the multidisciplinary drifting observatory for study of Arctic climate (MOSAiC). Case study events range from snowfall with highly rimed particles observed during periods with large amounts of supercooled liquid water path (LWP > 320 g m^{-2}) to unrimed snowflakes including instances when pristine planar crystals were the dominant frozen hydrometeor habit. The prefactor *a* and the exponent *b* in the observed $V_t–Z_e$ relations scaled to the sea level vary in the approximate ranges 0.5 – 1.4 and 0.03 – 0.13, respectively (reflectivities are in mm^6m^{-3} and velocities are in m s^{-1}). The coefficient *a* values are the smallest for planar crystals (a~0.5) and the largest (a>1.2) for particles under severe riming conditions with high LWP. There is no clear distinction between *b* values for high and low LWP conditions. The range of the observed $V_t–Z_e$ relation coefficients is in general agreement with results of modeling using fall velocity – size ($v_t =\alpha D^\beta$) relations for individual particles found in literature for hydrometeors of different habits, though there is significant variability in α and β coefficients from different studies even for a same particle habit. Correspondences among coefficients in the $V_t–Z_e$ relations for particle populations and in the individual particle $v_t–D$ relations are analyzed. These correspondences and the observed $V_t–Z_e$ relations can be used for evaluating different frozen hydrometeor fall velocity parameterizations in models.

Significance statement

Frozen hydrometeor fall velocities influence cloud lifecycles and the moisture transport in the atmosphere. The knowledge of these velocities is also needed to enhance remote sensing of snowfall parameters. In this study, the relations between fall velocities and radar reflecitivities of snowflakes of different types and shapes are quantitively analyzed using observations with vertically pointing radars.

Accepted for publication in *Journal of Applied Meteorology and Climatology*. DOI 10.1175/JAMC-D-23-0002.1.

1. Introduction

Hydrometeor terminal fall velocity information is important for weather and climate studies as it determines cloud life cycles and affects the vertical transport of moisture in the atmosphere. While fall velocities of liquid water drops as a function of their size/mass are relatively well known (Gunn and Kinzer 1949), frozen (ice) hydrometeor fall velocities are much more variable and, besides particle size, depend on other microphysical parameters including particle habit/shape and density (e.g., Mitchell 1996). Fall velocities are also influenced by environmental parameters (e.g., air density, turbulence). The parameterization of atmospheric ice fall speed emerged as one of the most important determinants of climate sensitivity (Flato et al. 2013). Uncertainties of frozen hydrometeor fall velocities are still significant, therefore sometimes scaling factors for existing fall velocity parameterizations are used in climate models to constrain both the global shortwave and longwave radiation to match the observed values (Hourdin et al. 2017).

The knowledge of frozen hydrometeor fall velocities is also important for development of quantitative precipitation estimation (QPE) methods for snowfall. Snowfall rate and ice water content (IWC) are related through fall velocities (e.g., Heymsfield et al. 2016). It allows for the use of existing IWC remote sensing methods to infer also estimates of snowfall rate thus providing more complete retrieval information. The fall velocity information provides a leverage for snowfall QPE through the use of advanced IWC retrieval approaches, including those, which utilize novel information from polarimetric weather radars (Ryzhkov et al. 2018).

Both modeling and direct observations have been used for developing hydrometeor fall velocity parameterizations. General aerodynamic considerations involving the drag coefficient calculations are typically used for theoretical developments. Modeling is usually performed for aggregates and different types of pristine crystals using empirical relations between particle sizes and masses as well as those between particle projected area ratios and sizes (e.g., Mitchell 1996; Heymsfield and Westbrook 2010; Schmitt et al. 2019). Fall velocities of frozen hydrometeors of different habits were also directly estimated near the ground using different in situ particle sampling sensors (e.g., Garrett and Yuter 2014; Vazquez-Martin et al. 2021). Such instantaneous estimates, however, are influenced by turbulence (e.g., Li et al. 2021), and wind (especially vertical air motions), which can result in increased measurement uncertainties (e.g., Fitch et al. 2021). Blowing snow also hinders ground measurements of falling snow (e.g., Schaer et al. 2020).

Since a number of weather and climate models nowadays provide estimates of such habit dependent hydrometeor parameters as radar reflectivity factor and fall velocity (e.g., Hashino and

Accepted for publication in *Journal of Applied Meteorology and Climatology*. DOI 10.1175/JAMC-D-23-0002.1.

Tripoli 2011; Jensen et al. 2017), the observational relations between these parameters for different particle habits can be used to improve representations of hydrometer sedimentation rates in models. Vertically-pointing Doppler radar measurements at different frequencies proved to be a useful tool for characterizing hydrometeor terminal velocities (e.g., Kropfli, et al. 1990; Gossard et al. 1992; Martner et al. 2002). Since observed Doppler velocities represent a sum of hydrometeor terminal velocities and vertical air motions, time averaging is usually used to minimize the air motion component (Orr and Kropfli 1999). The results are typically expressed as relations between the particle ensemble reflectivity-weighted terminal velocity, V_t, and the reflectivity factor, Z_e (hereafter just reflectivity). It was shown that the averaging interval of around 20 min provides a good compromise between minimizing the vertical air motion influence and the natural variability of the $V_t - Z_e$ relations due to changing particle microphysics (Protat and Williams 2011).

The main objective of this study was to investigate $V_t - Z_e$ relations using radar observations of Arctic snowfall. A combined analysis of these relations and concurrent estimates of frozen hydrometeor types and shapes (i.e., habits) from polarimetric radar measurements also allows for evaluation of how different snowfall processes that affect hydrometeor shapes (e.g., dendritic growth and subsequent aggregation) are manifested in fall velocity changes. Of interest to this study was also the investigation of $V_t - Z_e$ relation transitions due to particle riming (i.e., accretion and freezing of supercooled liquid on particle surface), observed during periods of increased amounts of supercooled liquid water in the vertical atmospheric column.

2. A brief description of the approach for deriving V_t - Z_e relations

The Doppler velocity, V_D, measured by a vertically-pointing radar represents a sum of vertical air motion, V_a, and the reflectivity-weighted terminal fall velocity of hydrometeors, V_t. The underlying assumption of the approach is that averaged over time small-scale vertical air motions are sufficiently small compared to frozen hydrometeor fall velocities, so in average terms $V_D \approx V_t$. This assumption was previously applied to cloud system measurements (e.g., Orr and Kropfli, 1999; Protat and Williams, 2011; Ye and Lee 2021). It is even more justifiable for snowfall, which is of main interest to this study, where precipitating hydrometeor fall velocities are usually higher than those in cloud systems that do not produce precipitation reaching the ground. Uncertainties of terminal fall velocities estimated using this approach are expected to be within 0.05 – 0.1 m s^{-1} (Orr and Kropfli 1999). A 20-minute time averaging was further used in this study. Reflectivity averaging is performed in the linear units (i.e., in mm^6m^{-3}).

Accepted for publication in *Journal of Applied Meteorology and Climatology*. DOI 10.1175/JAMC-D-23-0002.1.

The V_t–Z_e relations are derived for layers at different heights. For meaningful comparisons of the relations, the dependence of fall velocities on air density was approximately accounted for by referencing fall velocities to the mean sea level (MSL) as (Pruppacher and Klett 1997):

$$V_t(0) = V_t\,(h)\,[\rho_a(h=0)/\rho_a(h)]^{-0.43}\,, \quad (1)$$

where $V_t(h)$ is the radar-based fall velocity estimate at a height h above MSL, and ρ_a is the air density, which is obtained from radiosonde soundings of temperature and pressure using the ideal gas law. The use of $V_t(0)$ rather than $V_t\,(h)$ largely removes height dependences and allows for a more accurate consideration of hydrometeor habit influences on fall velocities.

Measurements of reflectivity and Doppler velocities used in this study were conducted with the U.S. Department of Energy's (DOE) Atmospheric Radiation Measurement (ARM) Program K_a-band (~ 35 GHz) zenith-pointing radars (KAZRs). Such radars are deployed at a number of permanent and mobile ARM facilities. In the general operation mode, ARM KAZRs have a gate spacing of 30 m, ~2 sec dwell time and a 1 km range sensitivity of about -35 dBZ. The lowest KAZR range gate, where measurements can be used for estimating reflectivity, is typically at an altitude of approximately 160 m above the ground. Applying the liquid cloud microphysical process calibration approach (Maahn et al. 2019) to radar measurements indicated that Oliktok and MOSAiC KAZRs were calibrated within few decibels for the measurement periods considered in this study (Matrosov et al. 2022a).

3. Results of deriving $V_t - Z_e$ relations

3.1. The Oliktok Point, AK, facility case studies

Frozen hydrometeor fall velocities are influenced by their shapes and types (Pruppacher and Klett 1997). Estimates of mean particle shapes as defined by their aspect ratios (i.e., the ratios particle minor-to-major dimensions) were available from polarimetric measurements by the Scanning ARM Cloud Radar (SACR). The fully polarimetric second version of this radar (SACR2) was deployed side-by-side with the KAZR at the Oliktok Point facility during some periods of the deployment of the ARM mobile facility (AMF3) at this location (Matrosov et al. 2020).

Nowadays many models account for several species of frozen hydrometeors (e.g., single crystals, aggregates, graupel). The cases considered in this study were aimed to cover instances when different species were dominant during extended periods of observations and concurrent radar data were available. The Oliktok Point 21 October 2016 event provided periods of confirmed layers of single planar crystals aloft as well as periods when irregular aggregates with limited

Accepted for publication in *Journal of Applied Meteorology and Climatology*. DOI 10.1175/JAMC-D-23-0002.1.

riming were a dominant species (Matrosov et al. 2017; 2020). The 11 November 2016 event was characterized by the extended period of very high values of supercooled liquid water path (LWP > 320 g /m^{-2}). Such large LWP values are considered to be an indicator of extreme riming and presence of graupel and heavily rimed particles (von Lerber et al. 2017).

Figures 1a and 1c depict time-height cross sections of KAZR measurements of reflectivity and mean vertical Doppler velocity (ARM user facility 2015) on 21 October 2016. The routine ARM measurements during the first three hours of this observational event were supported by in situ balloon-borne microphysical measurements aloft using National Center for Atmospheric Research's video ice particle sampler (VIPS) (Matrosov et al. 2017). The multi-angle snowflake camera (MASC) (Garrett et al. 2012) in situ images of falling hydrometeors near the ground during this event were among most frequent for the entire AMF3 deployment at Oliktok Point.

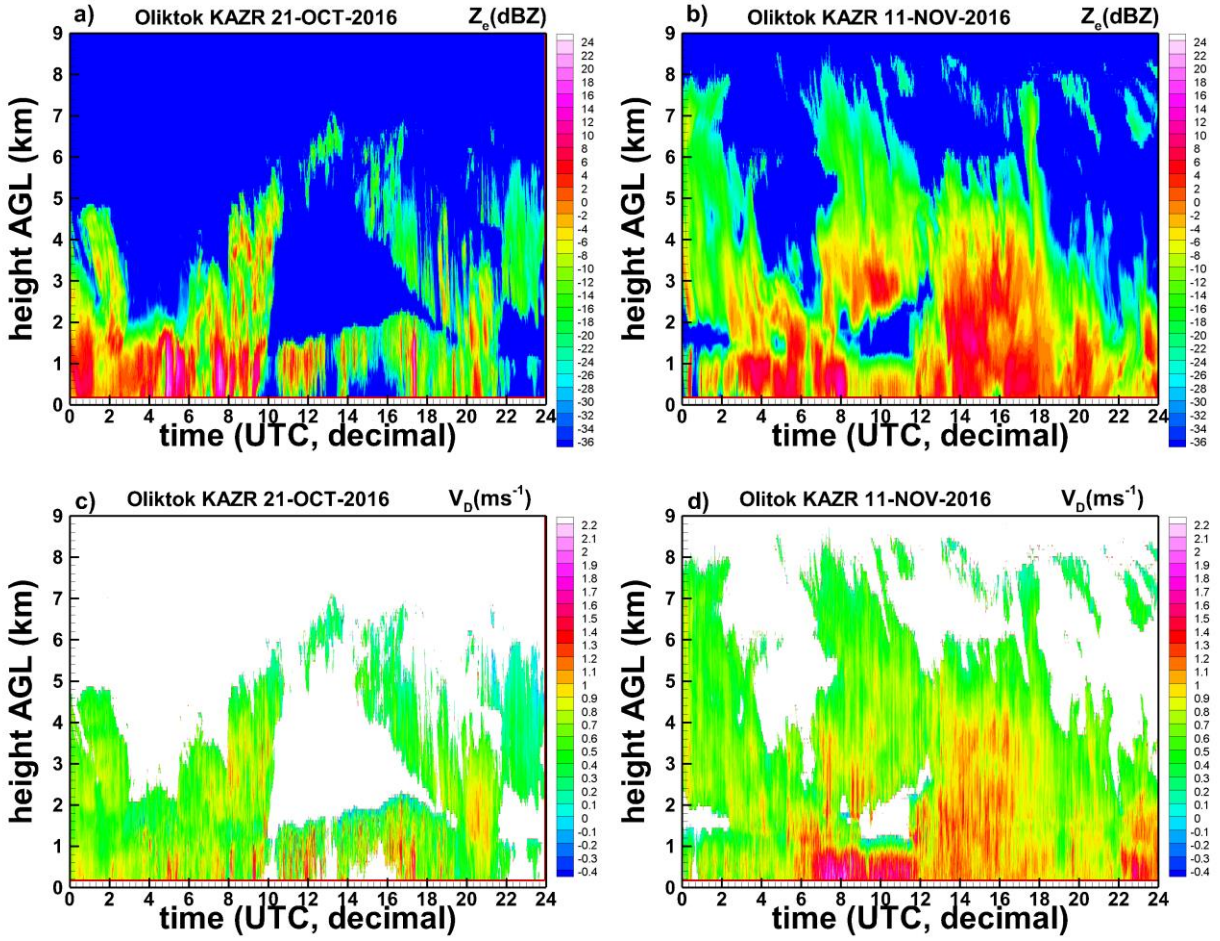

Figure 1. Time-height cross sections of Oliktok KAZR (a) and (b) reflectivities, and (c) and (d) mean vertical Doppler velocities for the events observed on (a), (c) 21-OCT-2016, and (b), (d) 11-NOV-2016.

Accepted for publication in *Journal of Applied Meteorology and Climatology*. DOI 10.1175/JAMC-D-23-0002.1.

Figure 2 shows results of particle aspect ratio retrievals from the SACR2 measurements. These retrievals were performed using range-height indicator (RHI) measurements of radar reflectivity, differential reflectivity and copolar correlation coefficient (ARM user facility 2016). These radar measurements were used to estimate circular depolarization ratio (CDR) which was then related to hydrometeor aspect ratios. The advantage of CDR-based retrievals of particle shapes is in smaller retrieval uncertainties caused by particle orientations. Details of the retrieval algorithm are presented in (Matrosov et al. 2017).

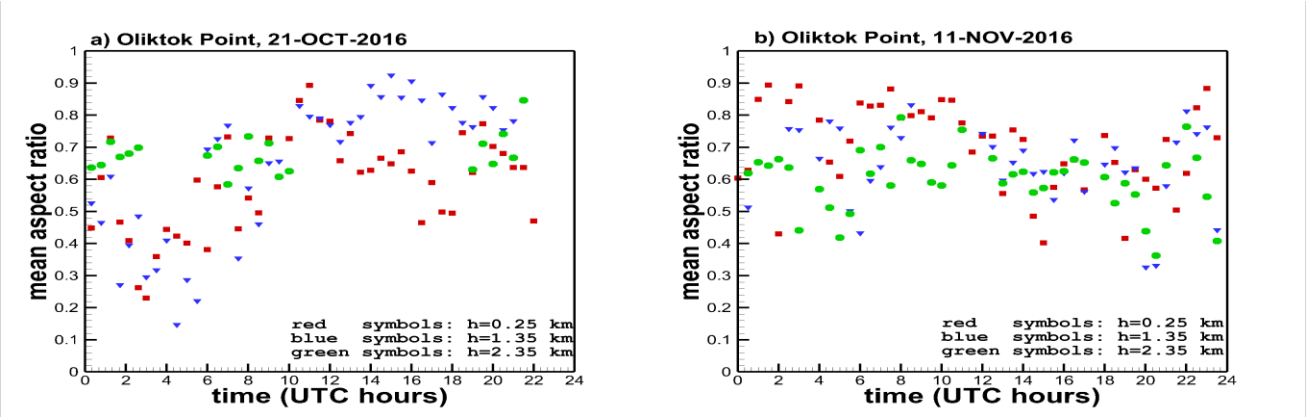

Figure 2. Time series of retrieved particle mean aspect ratios (a) for the 21 October 2016 and (b) for 11 November 2016 Oliktok Point events as retrieved from SACR2 measurements.

The retrievals were performed for eight different azimuthal directions at a radar beam elevation of 40°. For planar crystals, this elevation choice is a reasonable compromise between a need to retrieve aspect ratio vertical profiles and a diminishing sensitivity of radar-based particle shape retrievals when elevation increases (Matrosov et al. 2001). The azimuthal averaging of the results was performed at each height. The retrievals are available only during the 6-minute-long SACR2 RHI scan sequences, which were repeated every 30 minutes. Uncertainties of the aspect ratio retrievals were estimated as at least around 0.15 (Matrosov et al. 2017).

As seen from Fig. 2a, between about 2:00 and 6:00 UTC of the 21 October 2016 event, mean aspect ratios of observed ice particles were quite low, especially near the height of around 1.35 km above ground level (AGL). Radiosonde soundings (ARM user facility 2013) indicated that temperatures just above this height were around -15°C (Fig. 3a). This temperature regime favors the growth of oblate/planar pristine ice crystals types (e.g., Pruppacher and Klett 1997), such as dendrites, stellars and hexagonal plates, which have low aspect ratios. The dominance of single dendritic and plate type ice crystals during this particular time period was also confirmed

Accepted for publication in *Journal of Applied Meteorology and Climatology*. DOI 10.1175/JAMC-D-23-0002.1.

by in situ particle sampling (Matrosov et al. 2020), though some evidence of aggregation resulting in an increase of particle aspect ratios is evident at lower altitudes (Fig. 2a). Planar pristine crystals, however, are frequently not a dominant hydrometeor habit even at temperatures around -15°C as was a case during other time periods of the 21 October 2016 event (Matrosov et al. 2017).

The time series of dry bias corrected LWP and integrated water vapor (IWV) amount as retrieved from microwave radiometer data (ARM user facility 2014) for the event of 21 October 2016 are shown in Fig.4a. As can be seen from this figure, LWP during the 21 October 2016 event was generally relatively low except for several LWP spikes mostly in the time window between around 5:00 and 17:30 UTC. Since cloud supercooled liquid is the source of particle riming, only relatively light riming was expected outside this time period. This was confirmed by in situ particle sampling, which indicated no significant riming outside this time period but instances of particle riming after LWP spikes within this time period (e.g., Matrosov et al. 2020). Supercooled water temperatures generally varied between -5°C and -20°C (Matrosov and Turner 2018).

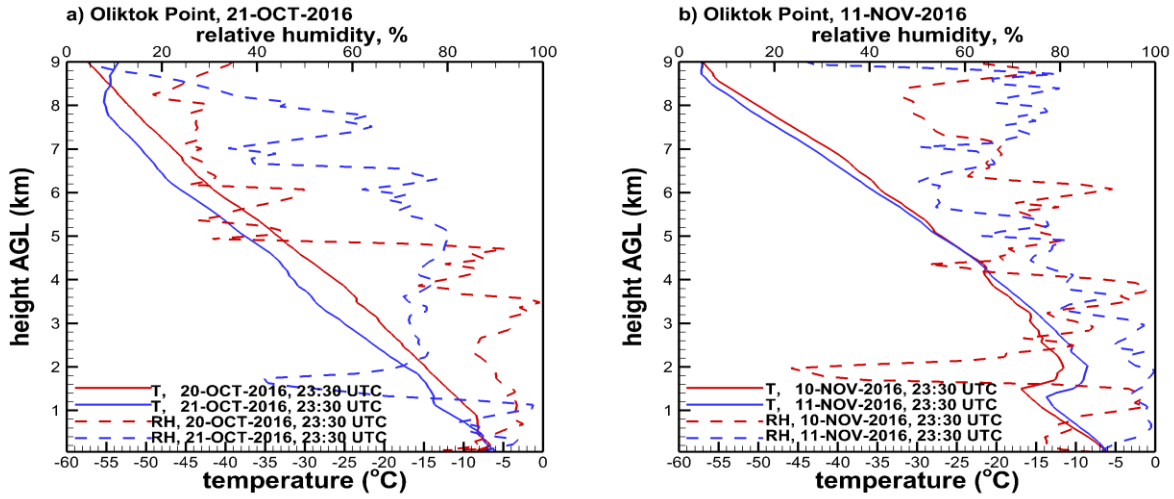

Figure 3. Radiosonde profiles for (a) for the 21 OCT 2016 and (b) for 11 NOV 2016 Oliktok Point events.

As customary accepted (e.g., Orr and Kropfli 1999), the V_t - Z_e relations were approximated by the power law:

$$V_t\ (\mathrm{ms^{-1}}) = \ a\ Z_e^{\,b}\ (\mathrm{mm^6 m^{-3}})\ . \qquad (2)$$

Figures 5a and 5b show V_t -Z_e relations derived from KAZR measurements on 21 October 2016 for the time period when single dendritic and plate type crystals were the dominant particle habit at a height of ~1.3 km (Fig. 5a), and during the time period of low LWP values between 17:30 and 22:00 UTC when relatively blocky aggregate particles with aspect ratios around 0.6 – 0.9 were observed at all heights (Fig. 5b). Corresponding root mean standard deviations (RMSD) of

Accepted for publication in *Journal of Applied Meteorology and Climatology*. DOI 10.1175/JAMC-D-23-0002.1.

observed velocities versus the best fit power law (2) are also shown. The relations were derived using the least squares method and linear reflectivity units (mm^6m^{-3}). To mitigate possible ground clutter effects, data with Z_e < -20 dBZ and $|V_D|$ < 0.05 m s^{-1} were not considered. Figure 5a also depicts examples of VIPS images (Matrosov et al. 2017) of typical particles observed aloft at heights where retrievals indicated lowest aspect ratios (Fig. 5a) and ground-based MASC images of spatial aggregate particles taken during the later time interval of low LWP values (Fig. 5b).

The mean particle aspect ratios and complexity parameters inferred from MASC images (Maahn 2019) during periods in Figs 5a and 5b were about 0.53 and 0.63 (for aspect ratios), and 1.82 and 1.92 (for complexities), respectively. The complexity parameter is defined by the ratio of the particle perimeter and the perimeter of the equivalent circle with accounting for the additional information from mean interpixel brightness variability (Garret and Yuter 2014). These authors indicate that the aggregated particles usually have complexity values greater than 1.75. Note that MASC aspect ratio data are inferred from particle projections, so they are generally greater than intrinsic aspect ratios.

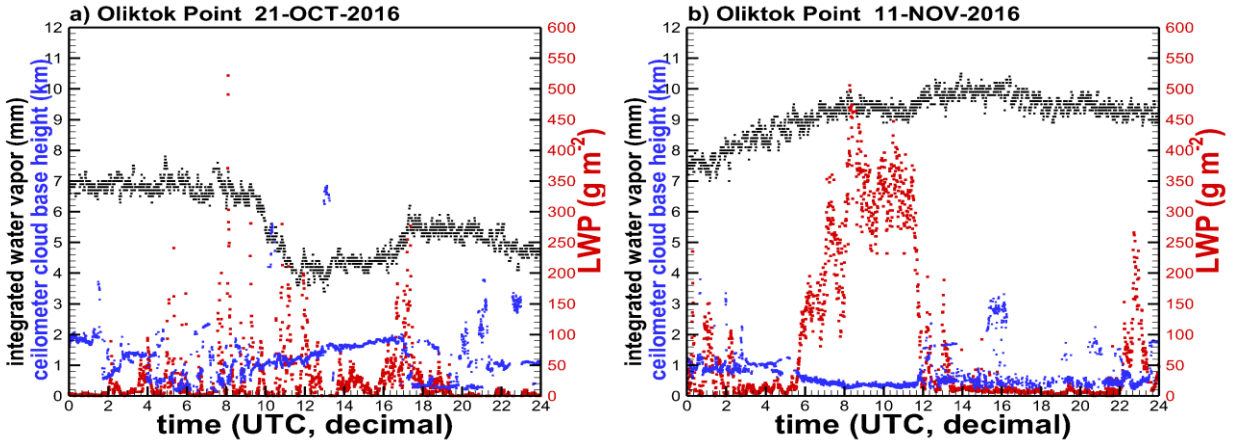

Figure 4. Time series of integrated water vapor (black), ceilometer cloud base (blue), and liquid water path (red) for (a) the Oliktok Point 21 October 2016 and (b) Oliktok Point 11 November 2016 events.

As seen from Fig. 5, the dependence of fall velocities on radar reflectivity is not very pronounced as the exponent *b* is relatively small. Especially small it is for dendritic and plate type crystals (Fig. 5a). The terminal fall velocity magnitudes of such crystals are smaller than for more rounded particles due a larger aerodynamic drag of more non-spherical particles, which tend to fall with their major dimensions oriented near horizontally (Matrosov et al. 2005). As a result, the exponent *b* in (2) for these pristine oblate crystals is noticeably smaller than that for particles with larger aspect ratios.

Accepted for publication in *Journal of Applied Meteorology and Climatology*. DOI 10.1175/JAMC-D-23-0002.1.

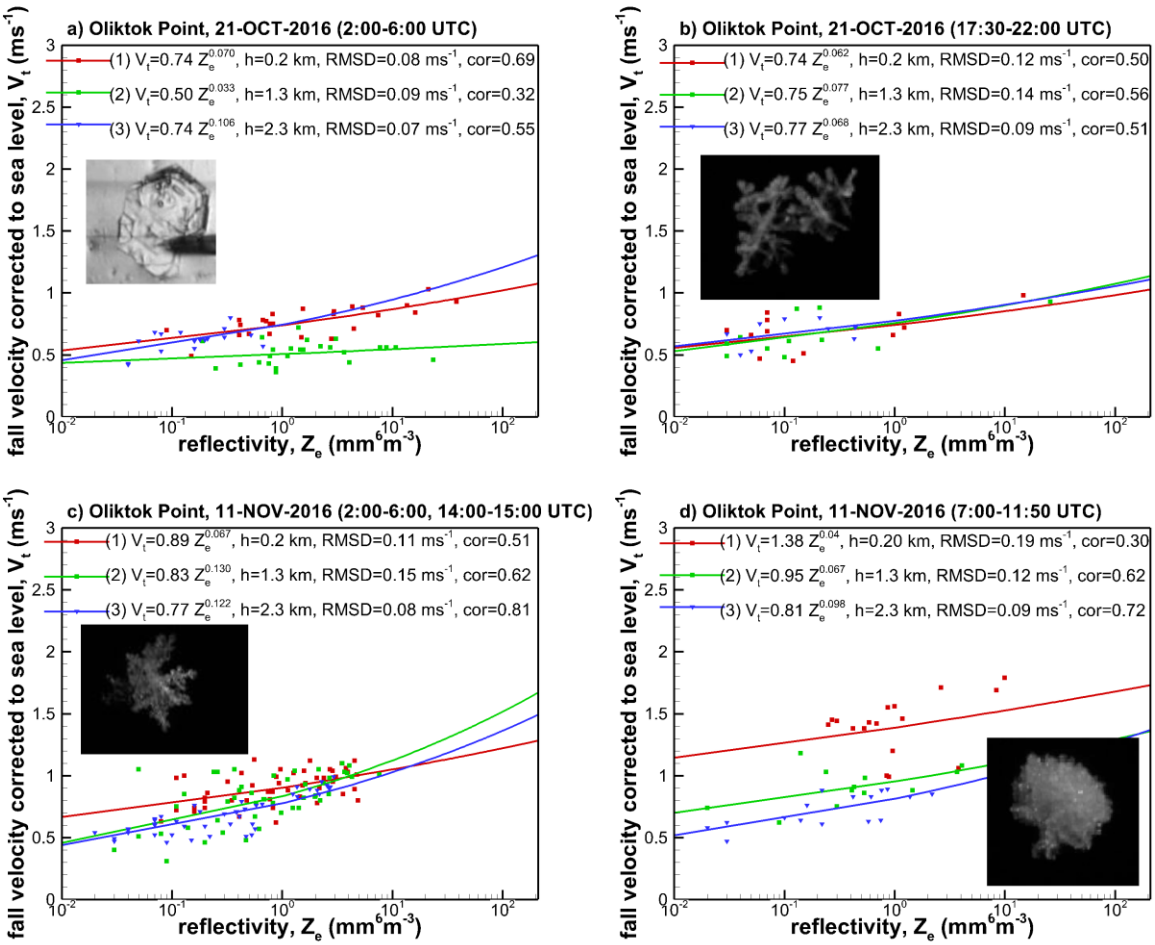

Figure 5. KAZR-based V_t-Z_e relations for the (a) and (b) the Oliktok Point 21-October 2016 event during (a) the prevalence of dendritic and plate type crystals near the height of 1.3 km and (b) during a period of mostly "blocky" particles with aspect ratios around 0.6 - 0.9 at all heights. Images of typical particles observed by the (a) VIPS aloft and (b, c, d) MASC at the ground. Frames (c) and (d) show V_t-Z_e relations for the Oliktok Point 11 November 2016 event during (c) low LWP values (<100 gm^2) and (d) during a period of high LWP values (> 320 gm^2). RMSD and correlation coefficient values are also shown.

The data shown in Figs. 5a and 5b mostly correspond to unrimed and/or only lightly rimed ice particles. Significant particle riming usually occurs when prolonged periods of high supercooled LWP values are present. Figures 1b and 1d show KAZR reflectivities and mean Doppler velocities for the Oliktok Point snowfall event observed on 11 November 2016 when periods of high LWP values were observed. SACR2-based retrievals of particle shapes indicated mean particle aspect ratios mostly in a range between approximately 0.5 and 0.9 (Fig.2b). In contrast to the initial several hours of the 21 October 2016 event, during the 11 November 2016 snowfall there were no pronounced height intervals where dendritic and plate type crystals were dominant even though according to radiosonde soundings favorable temperatures (i.e., -10^{o}C < t < -20^{o}C) were present between approximately 0.7 and 4.0 km AGL heights (Fig. 3b). As seen in

Accepted for publication in *Journal of Applied Meteorology and Climatology*. DOI 10.1175/JAMC-D-23-0002.1.

Fig. 2b, the dominance of ice particle populations with larger aspect ratios was characteristic for this snowfall (as well as the later hours of the 21 October 2016 event – Fig. 2a).

During the 11 November 2016 event, a rather prolonged time period of very high values of supercooled LWP was observed between approximately 7:00 and 11:50 UTC (Fig. 4b). Examples of ground-based MASC particle images (Maahn 2019) during this period are shown in Fig. 5d. During this period, the mean particle aspect ratio and complexity values inferred from MASC particle projections images were 0.65 and 1.33, respectively. Note that Garret and Yuter (2014) previously indicated that complexity parameter values less than 1.35 consistently correspond to graupel particles as riming tends to "round" and "smooth" hydrometeors.

As seen from Fig. 1d, this period of heavy riming due to the high supercooled liquid water content is also manifested in an increase of mean Doppler velocities in the lower atmospheric layer bellow approximately 1 km AGL. These velocities are often in excess of 1.5 ms^{-1}, which was shown to be an indicator of substantial riming of falling ice particles/snowflakes (Mosimann 1995; Vogel and Fabry 2018). It is interesting that the elevated Doppler velocities during the period of high LWP (Fig. 1d), on average, correspond to lower radar reflectivites (Fig. 1b) at similar AGL heights, which might indicate that these rimed particles are smaller in size and/or fewer in concentrations compared to snowflakes present during time periods with lower LWP values.

Figures 5c and 5d show the 11 November 2016 $V_t - Z_e$ relations inferred from the KAZR measurements for the time periods of low and high LWP values. The relations corresponding to low supercooled liquid amounts for the 21 October 2016 (Fig. 5b) and 11 November 2016 (Fig. 5c) events do not differ significantly from each other, which reflects the fact that similar estimates of particle terminal fall velocities are observed for the approximately same values of KAZR reflectivities. The radar-derived aspect ratios for these low LWP periods vary between about 0.5 and 0.9 (Figs 2a and 2b). The MASC mean particle aspect ratio and complexity for the low LWP 11 November 2016 period shown in Fig.5c were ~0.65 and 1.98, respectively, which are similar to those for the low LWP period of the 21 October 2016 event (Fig. 5b).

The upper height $V_t - Z_e$ relations in Fig. 5d are similar to those in Figs. 5a , 5b and 5c, which suggest that at those altitudes particle riming is limited. The lowest altitude $V_t - Z_e$ relation during the high LWP period on 11 November 2016 (Fig. 5d), however, stands out because it has a significantly larger prefactor coefficient *a* value compared to other relations, which is due to much higher fall velocities of heavily rimed particles.

Accepted for publication in *Journal of Applied Meteorology and Climatology*. DOI 10.1175/JAMC-D-23-0002.1.

3.2. MOSAiC expedition case studies

An ARM mobile facility was deployed onboard the icebreaker Polarstern as part of a year-long multidisciplinary drifting observatory for the study of Arctic climate (MOSAiC) (Shupe et al. 2021). The vertically-pointing ARM remote sensing instrumentation deployed at MOSAiC (e.g., the KAZR, ceilometer/radiometers) was similar to that at the Oliktok Point location. Polarimetric measurements from the scanning MOSAiC cloud radar provided linear depolarization ratio measurements only, so robust particle shape estimates aloft, similar to those obtained from the SACR2 fully-polarimetric ARM radar system, were not available. Nevertheless, it is instructive to analyze representative Central Arctic observational cases with low and high LWP values and compare them to the results from the Oliktok Point ARM facility for the cases with similar LWP amounts.

An important complication for the radar-based Doppler velocity measurements of falling frozen hydrometeors at MOSAiC was that the radar container on a drifting icebreaker was often not horizontally leveled due to the ship movements. Because of these movements, the radar beam was not exactly pointing vertically like in the case of the horizontally leveled ground-based radar platforms. As a result, there are non-zero projections of horizontal winds onto directions of the radar beam, which contaminate Doppler velocity measurements.

The horizontal winds can either increase or decrease intrinsic Doppler velocities depending on the horizontal wind speeds and directions and also on the icebreaker pitch, roll and yaw angles. The navigational information on these angles during the MOSAiC, however, was recorded, so the influences of the icebreaker movements can be quantitatively estimated. Unlike for Doppler measurements, the effects of the icebreaker movements were negligible on the reflectivity and height measurements since the deviations of the radar beam off vertical during the MOSAiC often did exceed a couple of degrees. The MOSAiC events, for comparisons with those from Oliktok Point, need to be chosen from the periods when icebreaker movements on radar Doppler information is minimized.

Figure 6 shows time-height cross sections of KAZR reflectivities and Doppler velocities for two contrasting MOSAiC snowfall events which had similar dynamic ranges of near ground reflectivities but quite different magnitudes of supercooled LWP. The radar data are available from the ARM user facility 2019a. The 16 November 2019 data (Figs. 6a and 6c) correspond to the warm sector of an Arctic cyclone (Matrosov et al. 2022a) during incursions of relatively warm and moist air. LWP values during this period were among the highest observed during the MOSAiC

Accepted for publication in *Journal of Applied Meteorology and Climatology*. DOI 10.1175/JAMC-D-23-0002.1.

first drift (i.e., mid October 2019 – mid May 2020) when practically all precipitation fell as snowfall. The lowest usable radar range gate of ~180 m AGL was high enough to mitigate effects of blowing snow, which often contaminated surface-based snowfall measurements during MOSAiC (Matrosov et al. 2022a).

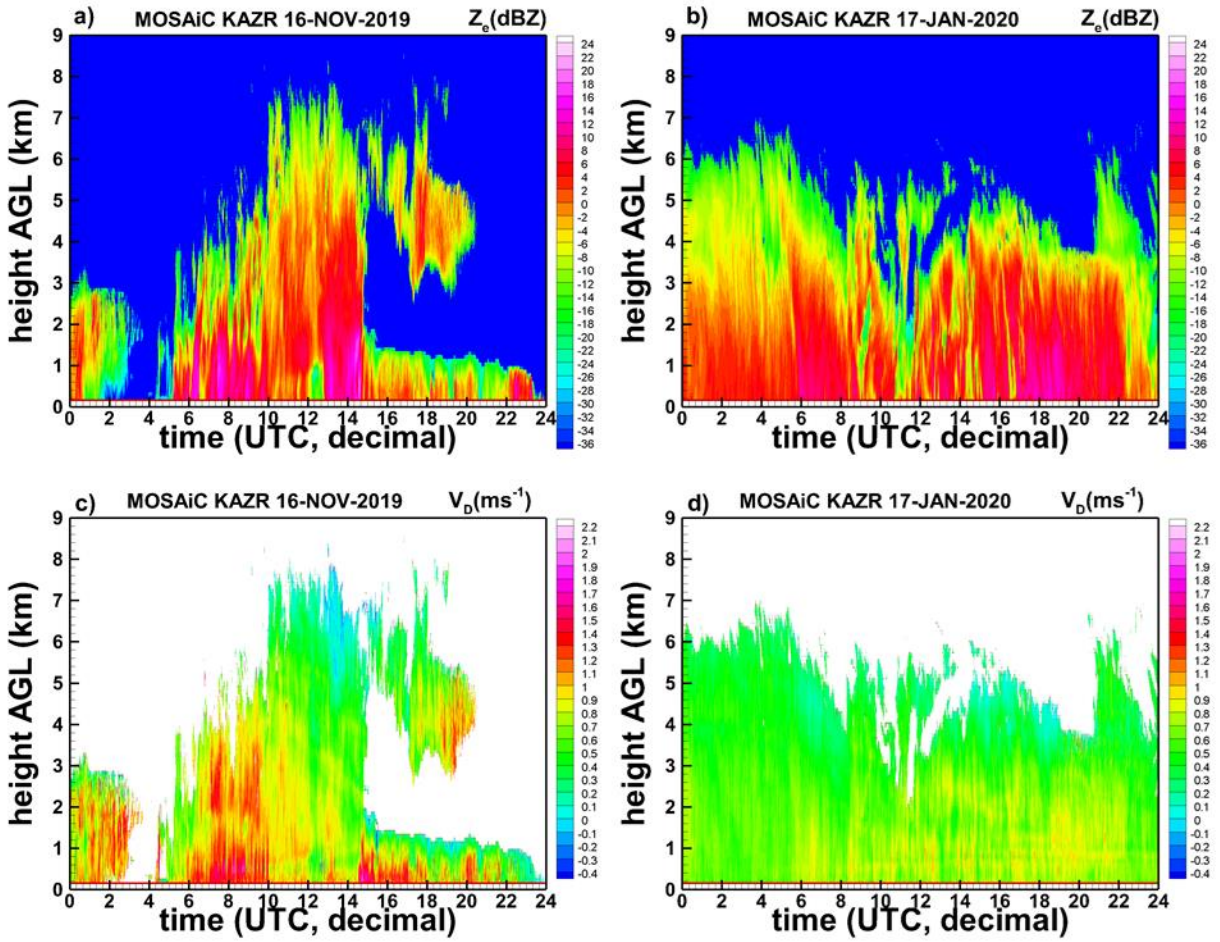

Figure 6. Time-height cross sections of MOSAiC KAZR (a) and (b) reflectivities, and (c) and (d) mean vertical Doppler velocities for the events observed on (a), (c) 16 NOV-2019, and (b), (d) 17-JAN-2020.

Figure 7 depicts liquid cloud base heights, integrated water vapor amounts and dry bias corrected LWP values retrieved from MWR measurements for the MOSAiC events shown in Fig.6 (ARM user facility 2019b). The time interval approximately between 15:30 and 21:00 UTC on 16 November 2019 when mean LWP values were higher than ~320 g m^{-2} (i.e., similar to that for the 7:00 - 11:50 UTC period during the Oliktok Point 11 November 2016 event – Fig. 4b) is of particular interest as some significant riming of falling hydrometeors is expected. The precipitating mixed-phase cloud during this time interval was rather shallow and detached from a higher altitude ice cloud (Figs. 6a and 6c).

Accepted for publication in *Journal of Applied Meteorology and Climatology*. DOI 10.1175/JAMC-D-23-0002.1.

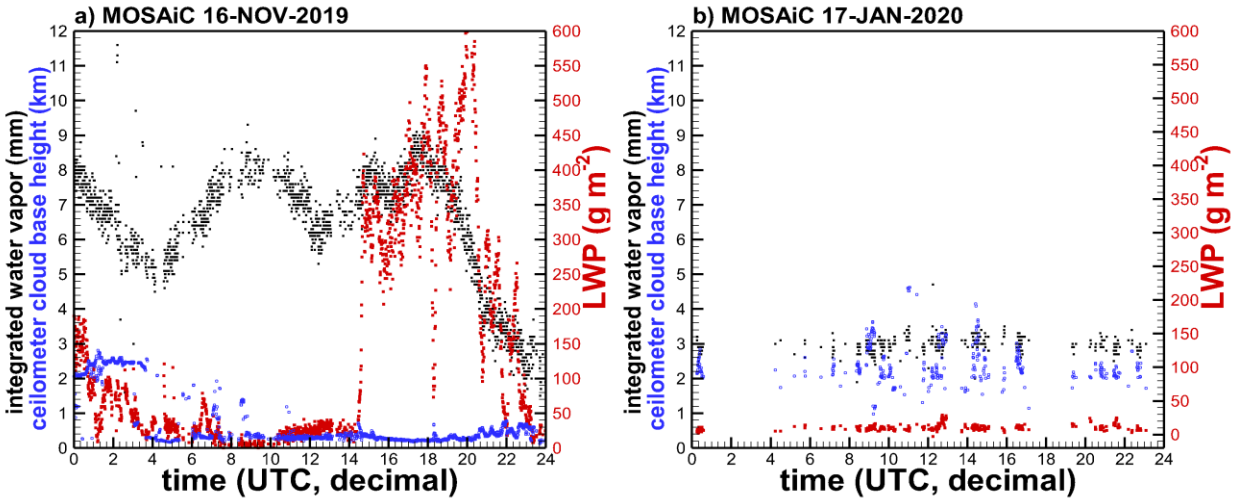

Figure 7. Time series of integrated water vapor (black), ceilometer cloud base (blue), and liquid water path (red) for (a) the MOSAiC 16 November 2019 and (b) 17 January 2020 events.

Figure 8 shows the MOSAiC icebreaker roll, pitch and yaw angles (ARM user facility 2019c) during the events shown in Fig. 6. The roll and pitch angles are positive for the starboard down and bow up ship movements. The yaw angle is relative to the geodesic north direction. While the yaw angle (unlike the pitch and roll angles) does not directly cause pointing of the radar beam being off vertical, it is important because the wind components in the ship roll and pitch planes depend on this angle. These horizontal wind components (i.e., V_r and V_p, correspondingly) can be approximately calculated as $V_h$sin(dir-yaw) and $V_h$cos(dir-yaw), where V_h and dir are the horizontal wind speed and direction, respectively. The temperature and horizontal wind data from radiosonde soundings (ARM user facility 2019d) for the events shown in Fig. 6 are depicted in Fig. 9.

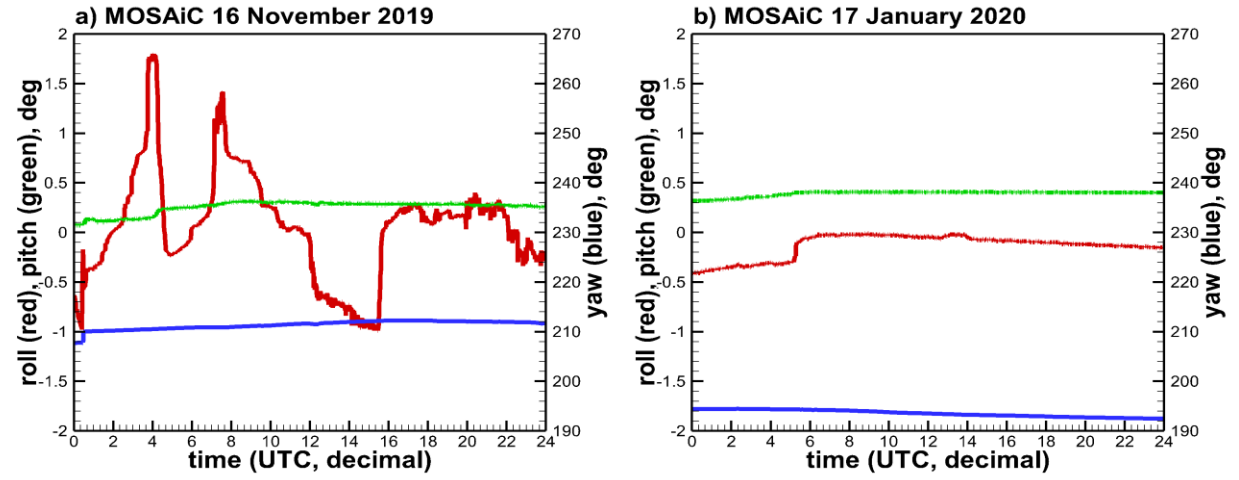

Figure 8. MOSAiC icebreaker movement angles during the MOSAiC (a) 16 November 2019 and (b) 17 January 2020 events.

Accepted for publication in *Journal of Applied Meteorology and Climatology*. DOI 10.1175/JAMC-D-23-0002.1.

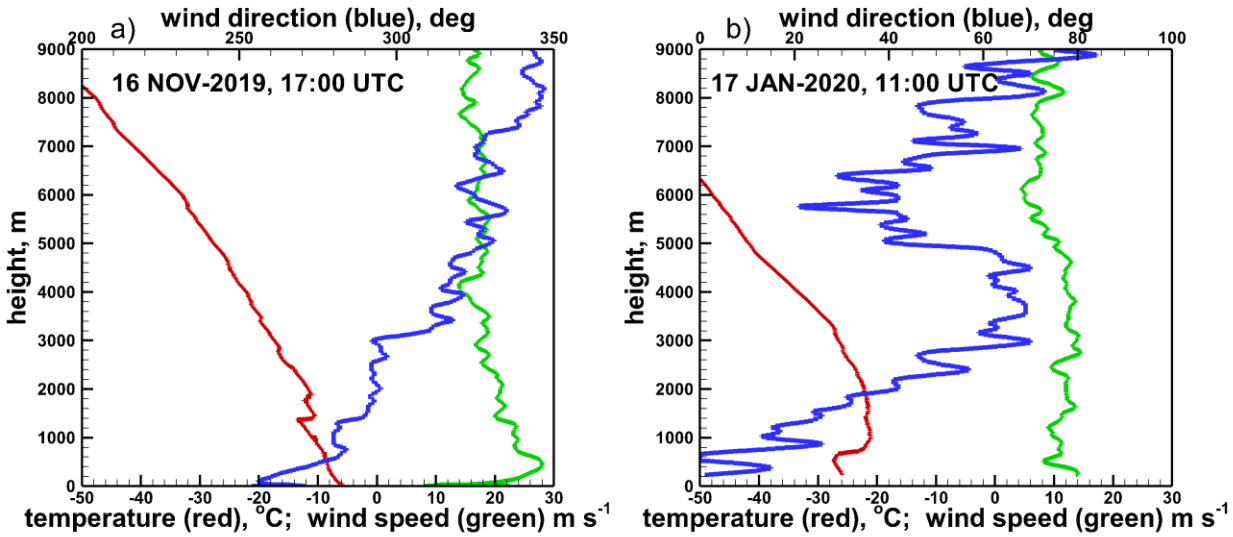

Figure 9. Radiosonde soundings for (a) 16 November 2019 and (b) for 17-January 2020.

For the yaw angles in Fig. 8a and wind directions in Fig. 9a, a positive roll angle would increase the observed Doppler velocity value by about $V_r$sin(roll) and a positive pitch angle would decrease this value by about $V_p$sin(pitch). As seen from Fig. 9a, horizontal wind speeds were relatively high (~25 m s^{-1}) for the entire vertical extent of the precipitating mixed-phase cloud with high LWP on 16 November 2019. The mean values of both the roll and pith angles, however, were positive and quite small (~0.2^o and ~0.3^o, respectively) between about 15:30 and 22:00 UTC. These combinations of icebreaker movements and horizontal wind parameters would result in approximate cancelations of horizontal wind contributions to Doppler velocity measurements (i.e., an approximate 0.07 m s^{-1} increase due to the ship roll and an approximate 0.06 m s^{-1} decrease due to the ship pitch). Outside this time period, the variability of the roll angle is considerable (Fig. 8a) though the pitch angle varies little and remains small. Larger positive/negative roll angles would cause a substantial general increase/decrease in observed Doppler velocities due to horizontal wind contributions.

Generally negligible horizontal wind influences on Doppler velocity measurements during the period of high LWP values observed on 16 November 2019 allow for the analysis of V_t –Z_e relations for this period. Figure 10a shows these relations for the height of ~0.2 km, which is approximately near the liquid cloud base (Fig. 7a) where riming is should be maximal, and also for the height of ~0.9 km, which is near the mixed-phase cloud top where little riming is expected.

Accepted for publication in *Journal of Applied Meteorology and Climatology*. DOI 10.1175/JAMC-D-23-0002.1.

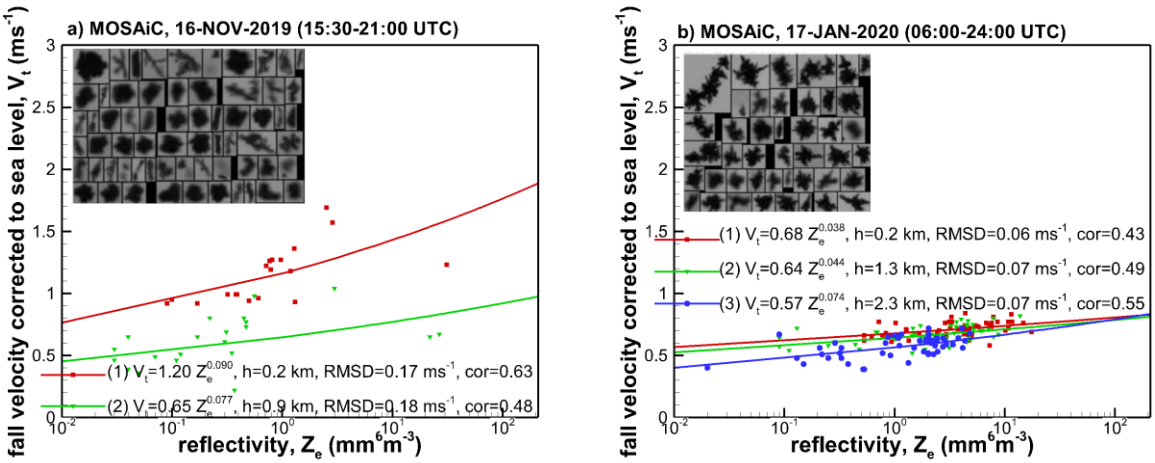

Figure 10. KAZR-based V_t-Z_e relations for (a) high LWP period of the MOSAiC 16 November 2019 event and (b) for the MOSAiC 17 January 2020 event with low LWP. RMSD and correlation coefficient values are also shown. Particle images are from Maahn et al. (2023).

As seen from Fig. 10a, rimed frozen hydrometeors near the ground fall considerably faster than particles near the cloud top. Typical images of particles observed at the ground by the Video In Situ Snowfall Sensor (VISSS) (Maahn et al. 2023) are also shown in Fig. 10. Although most of the particles (Fig. 10a) are blocky with rounded edges as could be expected for graupel-like hydrometeors, there are also some less rimed smaller particles. For particles at or near the ceilometer cloud base, the fall velocities during significant riming conditions with high supercooled LWP values are rather similar for the MOSAiC 16 November 2019 and the Oliktok Point 11 November 2016 events (Fig. 10a vs Fig. 5d). Typical V_t values for these conditions are in the range between 1.1 and 1.8 m s^{-1} for the reflectivity interval between 0 and 10 dBZ. For lower reflectivities, the velocities for the MOSAiC case are somewhat smaller compared to the Oliktok event which is likely due to contributions of smaller less rimed particles.

A MOSAiC snowfall event observed on 17 January 2020 (Figs. 6b, 6d) provided an opportunity to analyze fall velocities of frozen hydrometeors under condition of no or very limited riming. For this event, the columnar supercooled liquid amounts for the entire duration of the event were negligible (Fig. 7b). The range of radar reflectivity values, however, was similar to that observed during the 16 November 2019 MOSAiC event, though, at times, peak reflectivity values were higher for the 17 January 2020 observations. Temperatures during the 17 January 2022 event were generally colder than -20°C at all heights (Fig. 9b), so the dominance of planar crystals, which usually grow in the -10°C – -20°C temperature range (e.g., Pruppacher and Klett 1997), was not expected. More blocky particles with higher mean aspect ratios (~ 0.5 – 0.6) are typically observed

Accepted for publication in *Journal of Applied Meteorology and Climatology*. DOI 10.1175/JAMC-D-23-0002.1.

at temperatures colder than -20°C (Matrosov et al. 2020). Such particles were predominantly observed by the VISSS (Fig. 10b, insert) near the surface (Maahn et al. 2023).

The values of icebreaker pitch and roll angles (Fig. 8b) during the 17 January 2020 MOSAiC event were relatively small and did not exhibit significant variations (at least after 6:00 UTC). The horizontal wind speeds at heights between approximately 0.2 and 2.2 km were generally around 10 m s^{-1} (Fig. 9b). For these wind speeds and directions and also icebreaker movement angles, the contributions of horizontal winds into measured Doppler velocities are expected to be generally smaller than about 0.07 m s^{-1} or so, which is on the order of the fall velocity estimate uncertainties. These contributions were further neglected.

Figure 10b shows fall velocity – reflectivity relations for the negligible LWP period of 17 January 2020 MOSAiC event. As seen from this figure, there is not much variability in $V_t - Z_e$ relations at different heights. The strongest reflectivities at the lowest height of 0.2 km, however, are larger compared to those at higher altitudes. Particle size growth due to aggregation is one factor which might be responsible for the reflectivity increase.

Overall the $V_t - Z_e$ relations for the low LWP conditions during MOSAiC (Fig. 10b) are similar to those from Oliktok Point (e.g., Figs. 5b, 5c) though the prefactor a values in these relations are somewhat lower (by ~15%, on average) for the MOSAiC data. One exception is the period when pristine planar crystals such as dendrites, stellars and hexagonal plates were the dominant particle habit in the Oliktok Point observations. Standard deviations of individual $V_t - Z_e$ pair points relative to the best fit power law fit for MOSAiC observations are generally higher compared to Oliktok Point events. This can be explained, in part, by noisier Doppler velocity measurements from the icebreaker platform. Overall, RMSD values generally correspond to V_t standard deviations found by Protat and Williams (2011) for stratiform ice clouds.

3.3. Comparisons with previous estimations of $V_t - Z_e$ relations

Derivations of frozen hydrometeor $V_t - Z_e$ relations based on vertically pointing Ka-band radar measurements were previously conducted by Orr and Kropfli (1999) and more recently by Ye and Lee (2021). These authors, however, used measurements of mid-latitude ice clouds not resulting in snowfall near the ground. They did not specifically consider influences of hydrometeor habits and riming conditions on these relations. Orr and Kropfli (1999) generally focused on high ice clouds at lower temperatures (e.g., -30°C – -50°C), where particles are usually small. The

Accepted for publication in *Journal of Applied Meteorology and Climatology*. DOI 10.1175/JAMC-D-23-0002.1.

ranges of the power-law prefactor a and the exponent b in (2) in their study were 0.2 – 0.52 and 0.05 – 0.44, respectively.

Ye and Lee (2021) considered several ice cloud types. The prefactor coefficient a values according to their results varied generally between 0.4 and 0.9 for cirrus clouds and between 0.6 and 0.9 for anvils. Such values agree with prefactors found in this study for snow particles in low rime conditions except for the case when pristine planar crystals were dominant. The coefficient value for this case ($a \approx 0.5$) agrees better with results found previously for cirrus clouds. The prefactors for stratiform clouds were generally around 1, with some exception of when a reached a value of around 1.4. The exponent b values from (Ye and Lee 2021) varied in a range between approximately 0 and 0.2, which agrees well with the results for snow particles in this study.

While vertically pointing K_a-band radars are nowadays widely used for cloud and winter precipitation research, X-band (~10 GHz) radars also were utilized for measurements of vertical Doppler velocity changes associated with snowflake riming (e.g., Mosimann 1995; Vogel and Fabry 2018). Compared to mm-wavelengths, scattering at X-band is closer to the Rayleigh regime (Matrosov et al. 2022b), so observed X-band vertical Doppler velocities and reflectivities are larger. These X-band – K_a-band differences are important to consider when comparing vertical Doppler velocities from radars operating at different frequencies. To illustrate this point, Fig. 11a shows the ratio of expected Doppler velocities at X- and K_a-bands (i.e., $V_{tm}(X)/V_{tm}(K_a)$) when modeled V_{tm} values at a given frequency band were calculated as:

$$V_{tm} = \alpha \int_0^{D_{max}} N(D)\sigma(D)D^{\beta}\mathrm{d}D \Big/ \int_0^{D_{max}} N(D)\sigma(D)\mathrm{d}D\,, \qquad (3)$$

where the power-law approximation of the individual particle fall velocity – size relation (i.e., $v_t = \alpha D^{\beta}$) is assumed.

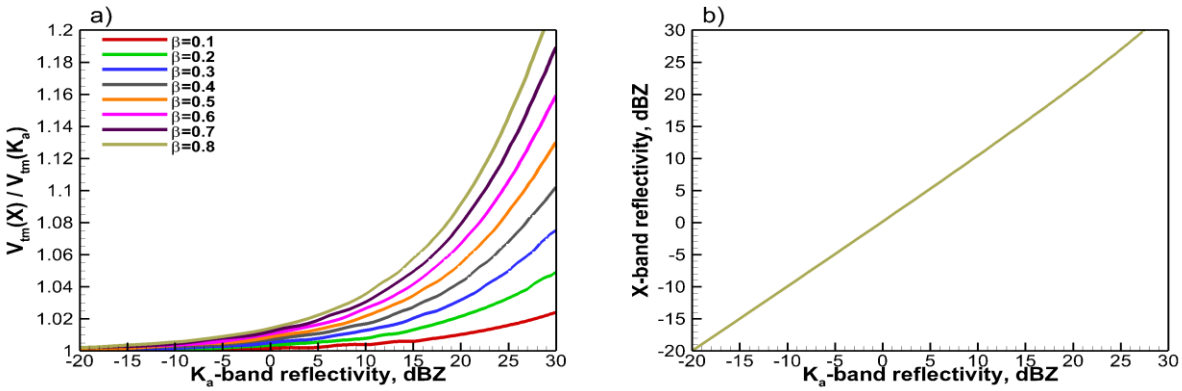

Figure 11. (a) Modeled fall velocity ratio $V_{tm}(X)/V_{tm}(K_a)$ as a function of reflectivity and (b) the mean correspondence between X and K_a-band reflectivities.

Accepted for publication in *Journal of Applied Meteorology and Climatology*. DOI 10.1175/JAMC-D-23-0002.1.

The backscatter cross sections of individual particles σ in (3) were calculated using the T-matrix method (Mishchenko et al. 2000) utilizing a generic assumption about the oblate spheroid snowflake aspect ratio of 0.6, which is often observed for irregular and aggregate frozen hydrometeors near the ground (e.g., Matrosov et al. 2020), and the particle mass – size relation m=0.0053 $D^{2.1}$, where m is individual particle mass in grams and D is its major dimension in centimeters (von Lerber et al. 2017; Matrosov and Heymsfield 2017). The T-matrix method was shown to adequately describe observed radar variables in snowfall including polarimetric ones (Matrosov 2021).

An exponential particle size distribution (PSD) $N(D)=N_0\exp(-3.67D/D_{mv})$ was assumed. In model calculations, the ice water content and the median volume particle size, D_{mv}, approximately varied from 0.01 to 2.5 g m^{-3} and from 0.4 to 3 mm, correspondingly. The maximum particle size, D_{max}, in the integration using (3) was assumed to be 1 cm. Note that the denominator of (3) represents a reflectivity value when multiplied by a factor of $\lambda^4\pi^{-5}|(\varepsilon+2)/(\varepsilon-1)|^2$, where λ and ε are the radar wavelength and the dielectric constant of water, respectively.

As seen from Fig. 11a, an increase in Doppler velocity values when observed at X-band (as compared to K_a-band) frequencies can be as large as 20% for higher reflectivity snowfalls. This (and also higher altitudes of radar measurements) can explain, in part, somewhat larger values of Doppler velocities observed for events with substantial riming in some previous studies which used X-band radar measurements (e.g., Mosimann 1995). Note that Mosimann (1995) in his study did not consider a general increase of hydrometeor mean fall velocities with increasing reflectivity. As seen from Fig. 11b, X-band reflectivities are also progressively higher than those at K_a-band for larger Z_e values which correspond to more intense snowfall consisting of larger falling hydrometeors.

The range of V_t values observed at lower altitudes during substantial riming cases in Figs. 5d and 10a (i.e., 1.2 – 1.8 m s^{-1} for the reflectivity interval between 0 and 10 dBZ) approximately corresponds to the range of 1.3 – 2.0 m s^{-1} if velocities were observed at altitudes 1.1 – 1.6 km MSL with an X-band radar (i.e., the setup of the Mosimann 1995 study) when the density dependence of terminal velocities and the K_a-band – X-band radar frequency differences are accounted for. According to Mosimann (1995), such Doppler velocities are typically observed for particles with a degree of riming of about 4 (i.e., heavy rimed frozen hydrometeors) and occasionally to particles with the highest degree of riming (i.e., 5).

Accepted for publication in *Journal of Applied Meteorology and Climatology*. DOI 10.1175/JAMC-D-23-0002.1.

4. Correspondence between $v_t - D$ relations for individual particles and $V_t - Z_e$ relations

Relations between individual particle fall velocities and their sizes (i.e., $v_t - D$ relations) were derived in a number of different observational and theoretical studies for various particle types (e.g., Locatelly and Hobbs 1974; Heymsfield and Kajikawa 1987; Mitchell 1996; Barthazy and Schefold 2006; Brandes et al. 2008; Lee et al. 2015; Vazquez-Martin et al. 2021) (hereafter L74, H87, M96, B06, B08, L15, V21). It is instructive to assess a consistency of the $V_t - Z_e$ relations derived in this study for particle ensembles with those $v_t - D$ relations obtained for individual particles. Theoretical estimates of the $V_t - Z_e$ relations obtained using (3) and corresponding to different values of the prefactor α and the exponent β in the individual particle $v_t - D$ relations are shown in Fig. 12. The α and β values for different ice particle types used for calculations of relations in Fig. 12 are shown in Table 1. The particle types are also shown in the Fig. 12 legends.

Table 1. Values of the prefactor α and the exponent β in the individual particle v_t–D relations used for deriving particle ensemble V_t–Z_e relations in Fig.12. Line **1**: Figure number (curve number); Line **2**: reference, Line **3**: α values, Line 4: β values (cgs units).

1:	12a(1)	12a(2)	12a(3)	12a(4)	12a(5)	12b(1)	12b(2)	12b(3)	12b(4)	12b(5)	12c(1)	12c(2)	12c(3)	12c(4)	12c(5)	12d(1)	12d(2)
2:	L74	V21	H87	L15	M96	H87	M96	L15	H87	H87	L74	L74	M96	B08	B08	B06	V21
3:	352	1070	613	1090	728	297	185	137	55	58	116	177	200	119	93	204	103
4:	0.37	1.00	0.89	0.94	0.79	0.86	0.56	0.24	0.48	0.55	0.16	0.41	0.42	0.25	0.23	0.22	0.37

Modeling results of $V_t - Z_e$ relations for graupel-like particles, which correspond to strong riming conditions (i.e., high supercooled LWP values), are presented in Fig. 12a. Calculations were performed assuming bulk density of 0.5 g cm^{-3} for these particles. This density is approximately in the middle of the graupel density expected range (Pruppacher and Klett 1997). Note that the constant density choice does not significantly affect the results because both the numerator and the denominator in (3) vary similarly when the particle density assumption changes. Comparing the observational $V_t - Z_e$ relations in Fig. 5d (line 1) and Fig. 10a (line 1), which correspond to the highly rimed particles, to the modeling results indicates that (given the observed RMSD values) measurements overall satisfactorily agree with some theoretical relations (shown by lines 4 and 5 and, particular, by line 1 in Fig. 12a). Both observational data and these theoretical relations suggest that near ground fall velocities of heavily rimed particles exceed a value of about 1 m s^{-1} when reflectivities are greater than approximately 1 mm^6m^{-3} (i.e., 0 dBZ).

Accepted for publication in *Journal of Applied Meteorology and Climatology*. DOI 10.1175/JAMC-D-23-0002.1.

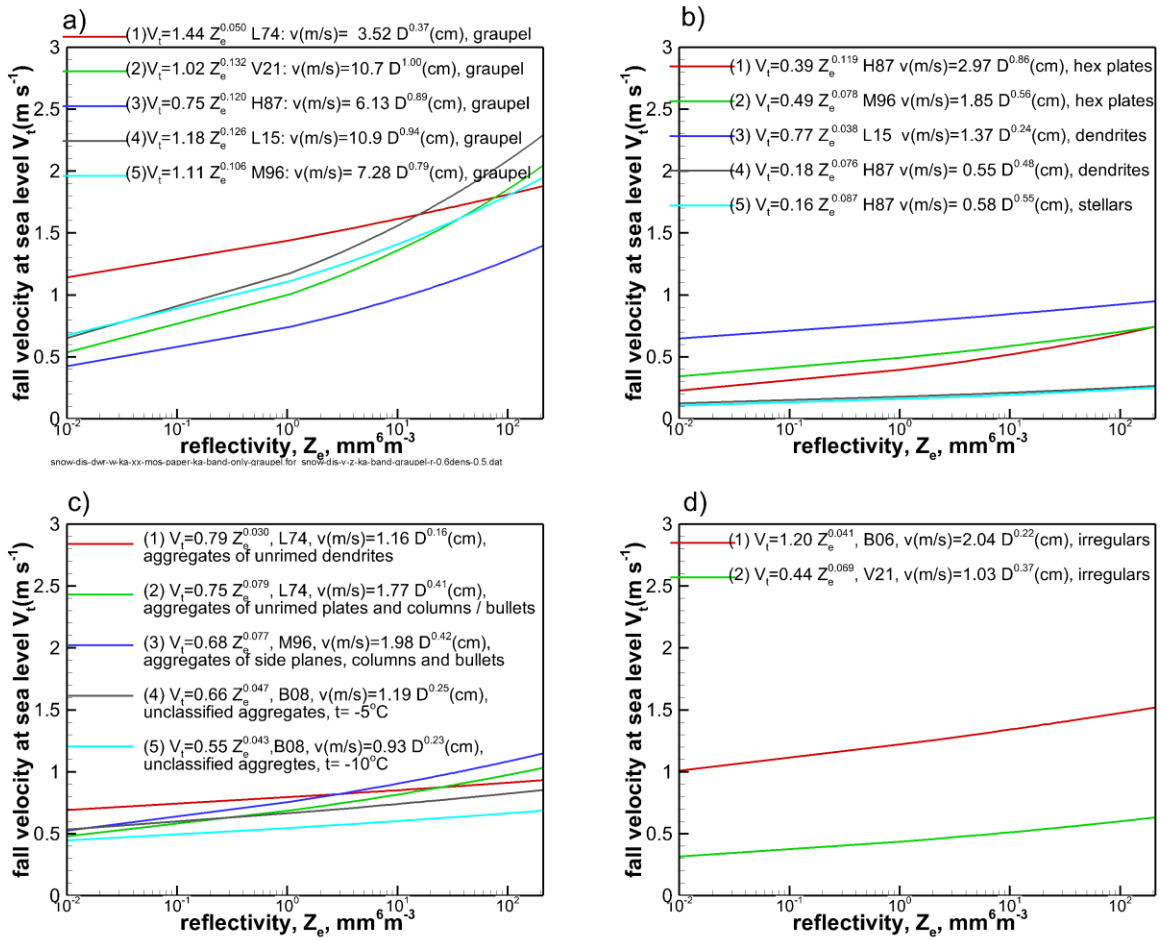

Figure 12. K_a-band modeled particle ensemble fall velocity–reflectivity (V_t–Z_e) relations for (a) graupel, (b) planar crystals, and (c and d) aggregate particles. The best fit power-law V_t–Z_e approximations are shown.

Figure 12b shows modeling results for pristine planar crystals. These results can be compared to the measurement data in Fig. 5a (line 2), which correspond to the time period and height (i.e., ~1.3 km) when such crystals were a dominant but not necessarily the only species present in the radar resolution volume. Modeling was performed assuming that the bulk density of planer crystals is given as $\rho(\text{g cm}^{-3})=0.588\ D^{-0.377}(\text{mm})$ (Pruppacher and Klett, 1997). A 0.2 particle aspect ratio was assumed, which is close to the retrieved values (Fig. 2a). The exact choice of the aspect ratio value does not significantly affect the results because (as for the case of the bulk density influence) of the mutual compensations in the numerator and the denominator in (3). As can be seen in Fig. 12b, the theoretical relations for planar crystals exhibit high variability depending on the α and β values from different studies. The observed $V_t - Z_e$ relations (Fig. 5a, line 2) for the case, when unrimed single planar crystals were a dominant habit, are approximately in the middle of the range of the theoretical data. Overall, reflectivity-weighted fall velocities of

Accepted for publication in *Journal of Applied Meteorology and Climatology*. DOI 10.1175/JAMC-D-23-0002.1.

planar crystals are smaller than those of graupel-like particles by a factor of larger than about 2 (for the same values of reflectivity).

Model calculations of the V_t – Z_e relations for aggregate hydrometeors for several individual particle v_t – D relations found in literature are shown in Fig. 12c. The modeled V_t – Z_e relations generally agree with the observed ones (Figs. 5b, 5c) from Oliktok Point when aggregates were a dominant hydrometeor habit and LWP was generally small. They are also in a relatively good agreement with the small LWP 17 January 2020 MOSAiC event when temperatures were lower (Fig. 10b). Results of some studies (e.g., Brandies et al. 2008) suggested temperature dependence of the v_t – D relations (Fig. 12c, lines 4 and 5), which affect the V_t – Z_e relations. Observational data here, however, did not indicate clear temperature dependent tendencies in V_t – Z_e relations as temperature changed with height (h < 2 km). Model calculations for irregular particles (Fig. 12d) indicate a large dynamic range of particle fall velocities.

Since both V_t and Z_e values increase when the radar frequency decreases (Fig. 11), it can be expected that the frequency change would not significantly affect the V_t – Z_e relations. Model calculations of these relations for the same hydrometeor types as in Fig. 12 were also performed for the X-band frequency (not shown). Comparing the K_a-band and X-band results indicated that the corresponding V_t – Z_e relations changed relatively little. Typical differences were generally within the uncertainty of hydrometeor velocity measurements (~0.05-0.1 ms^{-1}). Mixing different particle habits introduces additional uncertainties.

As seen from observations (Figs. 5 and 10) and model calculations (Fig. 12), the exponents in the particle ensemble V_t – Z_e relations are much smaller than those in the v_t – D relations for individual particles (Table 1). It can be explained by the fact that V_t is approximately proportional to the β-th PSD moment (i.e., eq. (3)), while reflectivity is proportional to the c-th moment. The value of c is 6 for the Rayleigh-size particles of the constant density and c is often as low as approximately 4 for particles when the exponent in the power-law particle mass - size relations is around 2. The exponent in the V_t –Z_e relations is approximately equal to the ratio of β/c, which is typically rather small. Note that the non-Rayleigh scattering effects also affect values of c.

Figures 13a and 13b show the power-law coefficients a and b in observed and modeled V_t –Z_e relations. Modeled values of a vary in a larger range compared to observational ones, though the variability ranges of b are very similar. Note also that coefficients in v_t – D relations as reported by various literature sources and used here for modeling vary significantly even for the same particle habit (Table 1 and Fig.13).

Accepted for publication in *Journal of Applied Meteorology and Climatology*. DOI 10.1175/JAMC-D-23-0002.1.

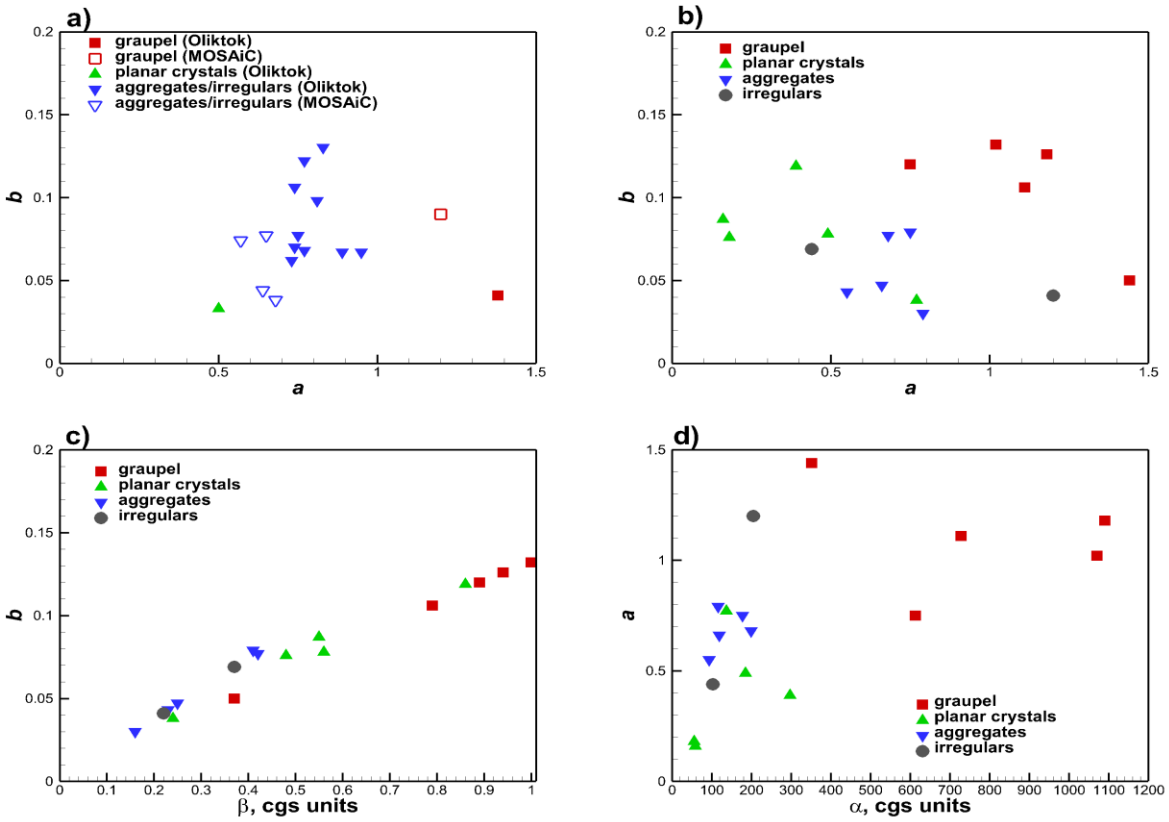

Figure 13: Correspondences between $V_t = aZ_e^b$ relation coefficients for (a) observed and (b) modeled data and correspondences between (c) modeled exponents β and *b* and (d) modeled prefactors α and *a* in the $v_t=\alpha D^{\beta}$ and $V_t=aZ_e^b$ relations for particle types in Table 1. Units of *a* and *b* are such that V_t and Z_e, are in m s^{-1} and mm^6m^{-3}, respectively.

Figures 13c and 13d depict modeled correspondences between α and β coefficients in the individual particles $v_t - D$ relations and those (i.e., *a* and *b*) in the particle ensemble $V_t - Z_e$ relations. It can be seen (Fig. 13c) that there is a significant correlation between values *b* and β. Note also that the correspondence between the exponents *b* and β does not depend on the prefactor α. The correspondence between *a* and α, however, depends on β. This correspondence is significantly less pronounced.

5. Conclusions

Vertically-pointing K_a-band Doppler radar measurements conducted in snowfall observed at the ARM mobile facilities at Oliktok Point, Alaska and in the central Arctic during the MOSAiC expedition were used to derive relations between reflectivity-weighted fall velocities and reflectivities (i.e., $V_t = aZ_e^b$ relations) scaled to the near surface air density. Time averaging of Doppler information was used to minimize influences of vertical air motions and turbulence on particle fall velocities. For MOSAiC snowfall periods considered in this study, deviations of the

Accepted for publication in *Journal of Applied Meteorology and Climatology*. DOI 10.1175/JAMC-D-23-0002.1.

radar beam from vertical pointing due to ship movements were minimal, so contributions of horizontal wind to observed Doppler velocities were small compared to particle fall velocities.

Since reflectivities are relatively well correlated with characteristic sizes of hydrometeor populations (Matrosov and Heymsfield 2017), the $V_t - Z_e$ relations are also indicative of the habit-dependent correspondence between fall velocities and characteristic sizes of particle populations. Note also that these relations show relatively little sensitivity to the radar absolute calibration because Doppler velocity measurements are immune to the absolute calibration errors and the exponent coefficients in these relations are small (i.e., ~ 0.03 – 0.14, in Figs., 5,10,12). Such small values of the exponent coefficients result in the V_t biases which are less than about 7% even if the reflectivity bias is around 2 dB.

Measurements were conducted in different snowfall conditions varying from the periods when single pristine planar crystals were a dominant hydrometeor habit to events with irregular aggregates with only traces of supercooled water presence and to environmental conditions favoring severe hydrometeor riming and forming graupel due to presence of large amounts of supercooled liquid in the vertical atmospheric column (> ~ 320 g m^{-2}). These varying hydrometeor habits corresponded to differing $V_t - Z_e$ relations.

Graupel-like particles formed as a result of severe riming are characterized by larger prefactor coefficients a in the $V_t = aZ_e^b$ relations for particle populations scaled to near surface air density (e.g., a > 1.1, when V_t is in ms^{-1}, and Z_e is in mm^6m^{-3}). The lowest values of a (~0.5) were observed when single planar crystals (e.g., dendrites, stellars, hexagonal plates) were dominant scatterers. Prefactor a values for irregular shape particle and aggregates typically varied between those for graupel and single planar crystals. These values for low LWP conditions were, on average, slightly smaller during MOSAiC observations compared to those at Oliktok Point, though the differences in a values between these two locations were generally within the standard deviation of the data scatter.

Values of the exponent b in the observed fall velocity – reflectivity relations generally varied between 0.03 and 0.14. These exponents are much smaller than exponents β in the individual particle fall-velocity size relations (i.e., $v_t = \alpha D^{\beta}$). There is a strong correlation between b and β, and the b – β correspondence is not affected by the values of the prefactor coefficient. Correlation between a and α is weaker than that between b and β.

The observed $V_t - Z_e$ relations were compared to the theoretical ones, which were modeled using individual particle fall velocity - size relations (i.e., $v_t = \alpha D^{\beta}$) found in literature for different

Accepted for publication in *Journal of Applied Meteorology and Climatology*. DOI 10.1175/JAMC-D-23-0002.1.

hydrometeor habits. There is, however, a significant variability in α and β coefficients (even for the same particle habits/species) when using the individual particle v_t - D relations from different previous studies. Overall, the prefactors a in the observed V_t – Z_e relations varied in a somewhat smaller range compared to the theoretical ones (i.e., ~ 0.5 – 1.5 vs ~ 0.2 – 1.5, when V_t is in ms^{-1} and Z_e in mm^6m^{-3}) especially for planar crystals. Variability ranges of b were approximately similar (i.e., ~ 0.03 – 0.14). Intercomparisons of observations and model calculations can be used as a consistency check tool for assessing individual particle fall speed – size relations used in different model studies.

Code and data availability. The Oliktok KAZR, MWR, radiosonde, and SACR2 data used in this study are available from the ARM archive at http://dx.doi.org/10.5439/1025214, http://dx.doi.org/10.5439/1566156, http://dx.doi.org/10.5439/1595321, and http://dx.doi.org/10.5439/1046197, respectively. The MOSAiC KAZR, MWR, navigation, and radiosonde data are available from the ARM archive at http://dx.doi.org/10.5439/1498936, http://dx.doi.org/10.5439/1027369, http://dx.doi.org/10.5439/1150247, and http://dx.doi.org/10.5439/1595321. T-matrix codes are freely available at https://www.giss.nasa.gov/staff/mmishchenko/t_matrix.html .

Financial support. This research was supported, in part, by the US Department of Energy (DOE) Atmospheric Systems Research (ASR) program projects DE-SC0022163 and DE-SC0013306. Additional support was provided by the NOAA Physical Sciences Laboratory through the cooperative agreement NA22OAR4320151.

References

ARM user facility. 2013. Balloon-Borne Sounding System (SONDEWNPN). ARM Mobile Facility (OLI) Oliktok Point, Alaska; AMF3 (M1). Compiled by K. Burk. ARM Data Center. Data set accessed 2020-12-12 at http://dx.doi.org/10.5439/1595321 .

ARM user facility. 2014. MWR Retrievals with MWRRET Version 2 (MWRRET2TURN). 2016-10-21 to 2016-10-22, ARM Mobile Facility (OLI) Oliktok Point, Alaska; AMF3 (M1). Compiled by K. Gaustad. ARM Data Center. Data set accessed 2020-12-12 at http://dx.doi.org/10.5439/1566156.

ARM user facility. 2015. Ka ARM Zenith Radar (KAZRGE). 2016-10-21 to 2016-11-11, ARM Mobile Facility (OLI) Oliktok Point, Alaska; AMF3 (M1). Compiled by N. Bharadwaj, I. Lindenmaier, Y. Feng, K. Johnson, D. Nelson, B. Isom, J. Hardin, A. Matthews, T. Wendler, V. Castro and M. Deng. ARM Data Center. Data set accessed 2020-12-12 at http://dx.doi.org/10.5439/1025214 .

ARM user facility. 2016. Ka-Band Scanning ARM Cloud Radar (KASACRHSRHI). 2016-10-21 to 2016-10-21, ARM Mobile Facility (OLI) Oliktok Point, Alaska; AMF3 (M1). Compiled by N. Bharadwaj, I. Lindenmaier, Y. Feng, K. Johnson, D. Nelson, B. Isom, J. Hardin, A. Matthews, T. Wendler, V. Castro and M. Deng. ARM Data Center. Data set accessed 2020-12-12 at http://dx.doi.org/10.5439/1046197.

ARM user facility. 2019a. Ka ARM Zenith Radar (KAZRCFRGE). ARM Mobile Facility (MOS) MOSAIC (Drifting Obs - Study of Arctic Climate); AMF2 (M1). Compiled by I. Lindenmaier, Y. Feng, K. Johnson, D. Nelson, B. Isom, A. Matthews, T. Wendler, V. Castro and M. Deng. ARM Data Center. Data set accessed 2020-12-12 at http://dx.doi.org/10.5439/1498936.

ARM user facility. 2019b. MWR Retrievals (MWRRET1LILJCLOU). ARM Mobile Facility (MOS) MOSAIC (Drifting Obs - Study of Arctic Climate); AMF2 (M1). Compiled by D. Zhang. ARM Data Center. Data set accessed 2020-12-12 at http://dx.doi.org/10.5439/1027369.

ARM user facility. 2019c. Navigational Location and Attitude (NAV). 2019-11-01 to 2019-11-02, ARM Mobile Facility (MOS) MOSAIC (Drifting Obs - Study of Arctic Climate); AMF2 (M1). Compiled by S. Walton. ARM Data Center. Data set accessed 2022-12-12 at http://dx.doi.org/10.5439/1150247.

ARM user facility. 2019d. Balloon-Borne Sounding System (SONDEWNPN). ARM Mobile Facility (MOS) MOSAIC (Drifting Obs - Study of Arctic Climate); AMF2 (M1). Compiled by K. Burk. ARM Data Center. Data set accessed 2022-12-13 at http://dx.doi.org/10.5439/1595321 .

Barthazy E., and R. Schefold, 2006: Fall velocity of snowflakes of different riming degree and crystal types. *Atmospheric Research*, **82**, 391-398.

Brandes, E. A., K. Ikeda, G. Thompson, and M. Schonhuber, 2008: Aggregate terminal velocities/ temperature relations. *J. Appl. Meteor. Climatol*., **47**, 2729-2736.

Fitch, K.E., C. Hang, A. Talaei, and T.J. Garrett, 2021: Arctic observations and numerical simulations of surface wind effects on Multi-Angle Snowflake Camera measurements. *Atmos. Meas. Tech*., 14, 1127–1142, https://doi.org/10.5194/amt-14-1127-2021

Accepted for publication in *Journal of Applied Meteorology and Climatology*. DOI 10.1175/JAMC-D-23-0002.1.

Flato, G., J. Marotzke, B. Abiodun, P. Braconnot, S.C. Chou, W. Collins, P. Cox, F. Driouech, S. Emori, V. Eyring, C. Forest, P. Gleckler, E. Guilyardi, C. Jakob, V. Kattsov, C. Reason and M. Rummukainen, 2013: Evaluation of Climate Models. In: Climate Change 2013: The Physical Science Basis. Contribution of Working Group I to the Fifth Assessment Report of the Intergovernmental Panel on Climate Change [Stocker, T.F., D. Qin, G.-K. Plattner, M. Tignor, S.K. Allen, J. Boschung, A. Nauels, Y. Xia, V. Bex and P.M. Midgley (eds.)]. Cambridge University Press, Cambridge, United Kingdom and New York, NY, USA.

Gunn, R., and G. Kinzer, 1949: The terminal velocity of fall for water droplets in stagnant air.J. Meteor., 6, 243 – 248.

Hashino, T., and G.J. Tripoli, 2011: The spectral ice habit prediction system (SHIPS). Part IV: box model simulations of the habit-dependent aggregation process. *J. Atmos. Sci*., **68**, 1142-1161. DOI: 10.1175/2011JAS3667.1

Jensen, A.A., J.Y. Harrington, H. Morrison, and J.A. Milbrandt, 2017: Predicting ice shape evolution in a bulk microphysics model. *J. Atmos. Sci*., **74**, 2081-2114. https://doi.org/10.1175/JAS-D-16-0350.1

Garrett, T.J., and S.E. Yuter, 2014: Observed influence of riming, temperature, and turbulence on the fallspeed of solid precipitation. *Geophys. Res. Lett.*, **41**, 6515–6522. doi:10.1002/2014GL061016.

Garrett, T. J., C. Fallgatter, K. Shkurko, and D. Howlett, 2012: Fall speed measurement and high-resolution multi-angle photography of hydrometeors in free fall, *Atmos. Meas. Tech.*, **5(11)**, 2625–2633, doi:10.5194/amt-5-2625-2012.

Gossard, E.E., R.G. Strauch, D.C. Welsh, and S.Y. Matrosov, 1992: Cloud layers, particle identification, and rain profiles from ZRV_f measurements by clear-air Doppler radars. *J. Atmos. Oceanic Technol*., **9**, 108-119. https://doi.org/10.1175/1520-0426(1992)009<0108:CLPIAR>2.0.CO;2

Heymsfield, A. J. and M. Kajikawa, 1987: An improved approach to calculating terminal velocities of plate-like crystals and graupel, *J. Atmos. Sci*., **44**, 1088–1099, https://doi.org/10.1175/1520-0469(1987)044<1088:AIATCT>2.0.CO;2, 1987.

Heymsfield, A.J., and C.D. Westbrook, 2010: Advances in the estimation of ice particle fall speeds using laboratory and field measurements. *J. Atmos. Sci*., **67**, 2469-2482.

Heymsfield, A.J., S.Y. Matrosov, and N.B. Wood, 2016: Toward improving ice water content and snow-rate retrievals from radars. Part I: X and W-bands, emphasizing *CloudSat*. *J. Appl. Meteor. Climatol.*, **55**, 2063-2090. https://doi.org/10.1175/JAMC-D-15-0290.1

Hourdin, F., and co-authors, 2017: The art and science of climate model tuning. *Bull. Amer. Meteor. Soc*., **98**, 589-602.

Kollias, P., Clothiaux, E. E., Ackerman, T. P., Albrecht, B. A.,Widener, K. B., Moran, K. P., Luke, E. P., Johnson, K. L., Bharadwaj, N., Mead, J. B., Miller, M. A., Verlinde, J., Marchand, R. T., and Mace, G. G.: Development and Applications of ARM Millimeter-Wavelength Cloud Radars, *Meteor. Mon*., **57**, 17.1–17.19, https://doi.org/10.1175/AMSMONOGRAPHSD-15-0037.1, 2016.

Accepted for publication in *Journal of Applied Meteorology and Climatology*. DOI 10.1175/JAMC-D-23-0002.1.

Kropfli, R.A., B.W. Bartram, and S.Y. Matrosov, 1990: The upgraded WPL dual-polarization 8-mm Doppler radar for microphysical and climate research [Preprints]. Conference on Cloud Physics. San Francisco, CA: American Meteorological Society: 341–345.

Leinonen, U., and W. Szymer, 2015: Radar signatures of snowflake riming: A modeling study. *Earth and Space Science*, **2**, 246–358, doi:10.1002/2015EA000102.

Lee, J., S.-H. Jung, H-M. Park, S. Kwon, P.-L. Lin, and G. Lee, 2015: Classification of precipitation types using fall velocity-diameter relationships from 2D-video distrometer measurements, *Adv. Atmos. Sci*., **32**, 1277–1290, https://doi.org/10.1007/s00376-015-4234-4 .

Li, C., K. Lim, Y. Berk, A. Abraham, M. Heisel, M. Guala, F. Coletti and J. Hong, 2021: Settling and clustering of snow particles in atmospheric turbulence. *J. of Fluid Mechanics*, **912**, A49. https://doi.org/10.1017/jfm.2020.1153

Lindenmaier, I., K. Johnson, D. Nelson, B. Isom, J. Hardin, A. Matthews, T. Wendler, and V. Castro, 2019: Ka ARM Zenith Radar (KAZRCFRGE). Atmospheric Radiation Measurement (ARM) user facility. doi: 10.5439/1498936.

Locatelli, J. D. and P.V. Hobbs, 1974: Fall speeds and masses of solid precipitation particles, *J. Geophys. Res*., **79**, 2185–2197, https://doi.org/10.1029/JC079i015p02185

Maahn, M., 2019: MASC snow particle images; ARM Mobile Facility (OLI) Oliktok Point, Alaska; AMF3 (M1). ARM Data Center, accessed 21 February 2019, https://doi.org/10.5439/1497701 .

Maahn, M., F. Hoffman, M.D. Shupe, G. de Boer, S.Y. Matrosov, and E. Luke, 2019: Can liquid cloud microphysical processes be used for vertically pointing cloud radar calibration? *Atmos. Meas. Tech*., **12**, 3151–3171.

Maahn, M. D. Moisseev, I. Stainke, N. Maherndl, and M. Shupe, 2023: Introducing the Video In Situ Snowfall Sensor (VISSS), Preprint egusphere-2023-655, https://doi.org/10.5194/egusphere-2023-655

Martner, B.E., B.W. Bartram, J.S. Gibson, W.C. Campbell, R.F. Reinking, and S.Y. Matrosov, 2002: An overview of NOAA/ETLs scanning K_a-band cloud radar. Preprints, *16th Conf. on Hydrology*, Orlando, FL, Amer. Meteor. Soc., 21–23.

Matrosov, S.Y., 2021: Polarimetric radar variables in snowfall at Ka- and W-band frequency bands: A comparative analysis. *J. Atmos. Oceanic Technol.*, **38**, 91-100. https://doi.org/10.1175/JTECH-D-20-0138.1

Matrosov, S. Y. and A.J. Heymsfield, A. J., 2017: Empirical relations between size parameters of ice hydrometeor populations and radar reflectivity, *J. Appl. Meteorol. Clim*., **56**, 2479–2488, https://doi.org/10.1175/JAMC-D-17-0076.1 .

Matrosov, S.Y., and D.D. Turner, 2018: Retrieving mean temperature of atmospheric liquid water layers using microwave radiometer measurements. *J. Atmos. Oceanic Technol.*, **35**, 1091-1102. https://doi.org/10.1175/JTECH-D-17-0179.1

Matrosov, S.Y., R. F. Reinking, R. A. Kropfli, B. E. Martner, and B. W. Bartram, 2001: On the use of radar depolarization ratios for estimating shapes of ice hydrometeors in winter clouds. *J. Appl. Meteor*., **40**, 479–490, https://doi.org/10.1175/1520-0450(2001)040<0479:OTUORD>2.0.CO;2 .

Matrosov, S.Y., R.F. Reinking, and I.V. Djalalova, 2005: Inferring fall attitudes of pristine dendritic crystals from polarimetric radar data, *J. Atmos. Sci*., **62**, 241-250, https://doi.org/10.1175/JAS-3356.1 .

Matrosov, S.Y., C. G. Schmitt, M. Maahn, and G. de Boer, 2017: Atmospheric ice particle shape estimates from polarimetric radar measurements and in situ observations. *J. Atmos. Oceanic Technol.*, **34**, 2569–2587, https://doi.org/10.1175/JTECH-D-17-0111.1.

Matrosov, S.Y., A.V. Ryzhkov, M. Maahn, and G. de Boer, 2020: Hydrometeor shape variability in snowfall as retrieved from polarimetric radar measurements *J. Appl. Meteor. Climatol.*, **59**, 1503-1517. https://doi.org/10.1175/JAMC-D-20-0052.1

Matrosov, S.Y., M.D. Shupe, and T. Uttal, 2022a: High temporal resolution estimates of Arctic snowfall rates emphasizing gauge and radar-based retrievals from the MOSAiC expedition. *Elementa: Science of the Anthropocene* **10(1).** https://doi.org/10.1525/elementa.2021.00101

Matrosov, S.Y., Korolev, A., Wolde, M., and Nguyen, C., 2022b: Sizing ice hydrometeor populations using the dual-wavelength radar ratio. Atmos. Meas. Tech., 15, 6373–6386, https://doi.org/10.5194/amt-15-6373-2022 .

Mishchenko, M., Hovenier, J.W., and Travis, L.D., 2000: Light Scattering by nonspherical particles. Academic Press.San Diego, 690 pp. ISBN 0-12-498660-9.

Mitchell, D.L., 1996: The use of mass- and area-dimensional power laws for determining precipitating particle terminal velocities. *J. Atmos. Sci*., **53**, 1710-1723.

Mosimann, L, 1995: An improved method for determining the degree of snow crystal riming by vertical Doppler radar. *Atmospheric Research*, **37**, 305-323.

Orr, B.W., and R.A. Kropfli, 1999: A method for estimating particle fall velocities from vertically pointing Doppler radar. *J. Atmos. Oceanic. Technol*., **16**, 29-37.

Protat, A., and C.R. Williams, 2011: The accuracy of radar estimates of ice terminal fall speed from vertically pointing Doppler radar measurements. *J. Appl. Meteor. Climatol*., **50**, 2120-2138.

Pruppacher, H.R., and J.D. Klett, 1997: Microphysics of clouds and precipitation, 2nd edition Kluwer Academic, Dordrecht, Holland, 954 pp.

Ryzhkov, A. P. Bukovcic, A. Murphy, P. Zhang, and G. McFarquhar 2018: Ice microphysical retrievals using polarimetric radar data. 10th European conference on radar in meteorology and hydrology, 1-6 July, Netherlands, pp. 494-504. https://edepot.wur.nl/454537.

Schaer, M., C. Praz, and A. Berne, 2020: Identification of blowing snow particles in images from a Multi-Angle Snowflake Camera. *The Cryosphere*, 14, 367–384, https://doi.org/10.5194/tc-14-367-2020

Schmitt, C.G., K. Sulia, Z.J. Lebo, A.J. Heymsfield, V. Przybyo, and P. Connolly, 2019: The fall speed variability of similarly sized ice particle aggregates. *J. Appl. Meteor. Climatol*., **58**, 1751-1761.

Shupe, M. D., M. Rex, K. Dethloff, E. Damm, A. A. Fong, R. Gradinger, C. Heuze, B. Loose, A. Makarov, W. Maslowski, M. Nicolaus, D. Perovish, B. Rabe, A. Rinke, V. Sokolov, A. Sommerfeld, 2020: The MOSAiC expedition: A year drifting with the Arctic sea ice. Arctic Report Card 2020, R. L. Thoman, J. Richter-Menge, and M. L. Druckenmiller, Eds. https://doi.org/10.25923/9g3v-xh92 .

Vazquez-Martin, S., T. Kuhn, and A. Eliasson, 2021: Shape dependence of snow crystal fall speed. *Atmos. Chem. Phys*., **21**, 7545–7565.

Vogel, J. M., and F. Fabry, 2018: Contrasting polarimetric observations of stratiform riming and nonriming events. *J Appl. Meteor. Climatol*., **57**, 457–476.

von Lerber, A., D. Moisseev, L. F. Bliven, W. Petersen, A. Harri, and V. Chandrasekar, 2017: Microphysical properties of snow and their link to Ze–S relations during BAECC 2014. *J. Appl. Meteor. Climatol*., **56**, 1561–1582.

Ye, BY., and GW. Lee, 2021: Vertical structure of ice clouds and vertical air motion from vertically pointing cloud radar measurements. *Remote Sens*., **13**, 4349. https://doi.org/10.3390/rs13214349